

Flexural Strength-Ductility Assessment of Unreinforced Masonry

Cross-Sections: Analytical Expressions

Nicola Giordano^{a,*} (nicola.giordano@polimi.it), Pietro Crespi^a (pietro.crespi@polimi.it), Alberto Franchi^a (alberto.franchi@polimi.it)

^a Department of Architecture, Built Environment and Construction Engineering, Politecnico di Milano, Piazza Leonardo da Vinci 32, 20133 Milano, Italy.

* Corresponding author. Tel.: +39 022399 4348. E-mail address: nicola.giordano@polimi.it. Postal address: Piazza Leonardo da Vinci 32, 20133 Milano, Italy.

ABSTRACT

The unreinforced masonry (URM) is a complex and variegated construction material characterized by a prominent nonlinear response. For this reason, advanced numerical simulations are required to assess URM buildings, especially in case of severe loading conditions as earthquakes.

However, given the theoretical and computational difficulties of detailed non-linear analyses linear elastic methods are still adopted in current practice. This results in conservative seismic assessments and, consequently, invasive and expensive strengthening interventions to guarantee seismic safety.

Starting from these statements, the aim of the paper is to provide closed-form equations useful for a preliminary strength and ductility assessment of unreinforced masonry rectangular cross-sections.

Expressions for direct calculation of $M-N$ (bending moment – axial load) strength domains and $M-\chi$ (moment – curvature) ductility curves for different constitutive laws are provided. The expressions are firstly applied to a representative URM cross-section and secondarily used for the numerical simulation of a recent out-of-plane loading experimental test available in the literature. For a better comprehension of the behavior of URM members in axial-bending load condition, 3D $M-N-\chi$ diagrams are presented in the paper.

Keywords

URM cross-section; seismic assessment; strength domain; moment-curvature, 3D $M-N-\chi$ diagram.

1. Introduction

Recent seismic events (L'Aquila Earthquake, Italy 2009 [1], Emilia Earthquake, Italy 2012 [2], Napa Earthquake, California 2014 [3]) have demonstrated another time that existing masonry buildings are affected by significant structural deficiencies. Poor quality of the materials, geometrical irregularities, inadequate wall-to-wall connections and absence of anti-seismic detailing are just a few aspects of masonry constructions weaknesses. Over the last years, the technical-scientific community has paid serious attention to the problem focusing on two main research lines. (i) Experimental investigation of the structural response of masonry before and after the application of strengthening interventions, both as prior-strengthening and as repair methods after damage. (ii) Development of analytical and numerical tools suitable for the seismic assessment and retrofitting design process of URM structures.

On one hand, the large amount of experimental tests carried out on masonry constructions [4] has allowed qualitative and quantitative validations of strengthening techniques (i.e. mortar injections, carbon-fiber reinforcements, tie-rods installation, floor-diaphragm strengthening, etc.) and calibration of masonry stress-strain constitutive models. On the other hand, the reliability of seismic assessment methods for URM buildings is still matter of debate [5], as recently observed in a blind test predictions experimental project carried out by Mendes et al. [6]. As a matter of fact, the usual hypotheses adopted in the structural analysis of reinforced concrete (r.c.) and steel buildings are no longer valid for masonry as briefly reported in Table 1.

	GENERAL STRUCTURES	MASONRY STRUCTURES
Material / structural components behavior in Service Limit State (SLS) conditions	Linear elastic.	Linear elastic response in compression. Very low resistance in tension (no-tension material assumption).
Material /structural components behavior in Ultimate Limit State (ULS) conditions	In general, it is possible to adopt elastic-plastic constitutive models in tension / compression. Structural component damages are usually concentrated in plastic hinge regions.	Material behavior in compression is characterized by a softening branch. Structural components can lead to collapse for bending damage, shear damage or loss of equilibrium.
Modelling	The structure (usually a 3D frame) is represented by a beam finite element model.	The structure is composed by a masonry continuum which, in some cases, cannot be discretized as a system of beam elements.
Type of analysis	Response Spectrum Analyses (RSA) are recommended by codes and guidelines.	Since elastic analyses cannot estimate the redistribution of stresses due to cracking, nonlinear methods are required.
Behavior under seismic actions	Global behavior is guaranteed by good node connections between structural elements.	In case of poor wall-to-wall / wall-to-floor connections, extensive cracks and damages can lead to the collapse of entire portions of the building (collapse mechanism).

Table 1. Usual hypotheses in the assessment of general structures and differences from masonry structures.

Lourenço et al. [7,8] furthermore underlined how the problem of knowledge is central when we are dealing with the seismic assessment of existing masonry constructions. In most cases the building geometry implemented in the structural software is not supported by a precise survey. Also, the internal composition of the walls cannot be investigated in an exhaustive way because of historic conservation prescriptions. Moreover, the characterization of the mechanical properties of the materials is challenging and requires expensive in-situ tests (flat jacks, diagonal compression, non-destructive tests, etc. [9,10]). Finally, especially for historic buildings, the material state of stress is influenced by the variability of the mechanical properties, by the construction stages and by the continuous human modifications and repairing interventions occurred during the life of the structure [11].

Depending on typology of the building, availability of mechanical and geometrical data and expected computational-cost, different seismic assessment approaches have been proposed in the literature:

- *Macro-Element Method or Equivalent Frame Method*. The building is subdivided into beam elements (piers and spandrels) connected in the intersections with rigid nodes. The deformable elements are characterized by in-plane behavior and the non-linear response is concentrated in appropriate plastic hinges that take into account the geometry of the masonry member and the mechanical properties of the material in shear and compression (Lagomarsino et al. [12]).

- *Continuum Finite Element Method (FEM)*. When the structure is characterized by a complex geometry, it is hard to adopt an equivalent frame simplification. In these cases, advanced FEM models with 2D/3D elements are preferred. Usually three approaches are adopted. I) Detailed micro-modelling: bricks and mortar joints are represented by continuum elements. II) Simplified micro-modelling: bricks are modeled by continuum elements while the behavior of the mortar joints is lumped in discontinuous interface elements. III) Macro-modelling: bricks and mortar are smeared out in a homogeneous continuum [7].

- *Discrete Element Method (DEM)*. The masonry structure is subdivided in a discrete number of rigid bodies. The methodology is formulated in large displacement and enables finite displacements and rotations of these bodies including complete separation; new contacts are also caught by the method (Lemos [13]).

The above mentioned techniques have been continuously developed and compared by academic researchers [14,15]. Despite that, consulting engineers and practitioners are loath to adopt complex non-linear methods. High computational costs, complex theoretical aspects, questionable interpretation and validation of the results, are just a few of the problems underlined in current practice. Unfortunately, the effect of these perplexities results in an improper use of linear elastic analyses that cannot catch the unavoidable cracking response of the masonry under seismic loads [16].

1.1. Assessment of URM cross-sections: literature review

Generally speaking, damages in URM components are a combination of three physical phenomena [17,18]: cracking of the resisting cross-section and toe compression failure generated by bending moment; bed joint sliding produced by shear forces; diagonal cracks due to shear actions. However, in case of slender masonry elements (such as columns, walls in out-of-plane loading, slender piers in in-plane loading, etc.), the leading failure mode is the one governed by bending. It is important to underline that the crisis at the sectional level (toe compression failure) can be preceded by the loss of equilibrium of the masonry element. This phenomenon occurs when the compressive strength of the masonry assemblage is relatively high or when the vertical stress due to dead loads is low.

Given this range of applicability, since '70ies [19] researchers have developed beam-theory based calculation tools able to predict the seismic capacity of URM elements. These studies, on one hand gave the starting point for the equivalent frame method formulation [20], on the other hand evolved

in a specific research line focused on the evaluation of the in-plane and out-of-plane capacity of URM members via non-linear cross-section analysis [21,22].

The principal assumption of the cross-section analysis is that axial strains behave linearly in bending i.e. sections remain plane. The advantages and the limitations of this hypothesis has been deeply discussed and validated [16,23,24]. Looking at the experimental data collected by Brencich et al. [25] and Cavaleri et al. [26], the plane section assumption better fits in case of slender walls, regular masonry blocks and absence of rubble masonry internal leaf.

Results of the cross-section analysis are usually summarized in two diagrams: the $M-N$ (bending moment - axial load) interaction curve reports the strength limit of the section; the $M-\chi$ (bending moment - flexural curvature) curve describes the deformation capacity of the section for a given axial load or eccentricity. Due to the complexity of the masonry material behavior, the analytical derivation of the $M-N$ and $M-\chi$ diagrams is matter of interest for the scientific community.

In 2013 Parisi et al. [23] evaluated $M-N$ strength domains for different masonry constitutive models. In their study $M=f(N)$ closed-form equations for parabola-rectangle EC6 law [27] are firstly derived. Then, the effect of strain-softening is investigated adopting two advanced masonry models by Turnšek-Čačovič [28] and by Augenti-Parisi [29]. Depending on the complexity of the analytical problem, the resulting $M-N$ curves are described by closed-form expressions or by a set of non-linear equations solved numerically.

The analytical estimation of $M-\chi$ curves has been investigated mainly for the case of constant eccentricity of the axial load. La Mendola [30] derived moment-curvature diagrams adopting the stress-strain softening model by Naraine et al. [31]. In their work, the nonlinear equations that define the equilibrium and compatibility of the cross-section are solved using an iterative numerical procedure. A similar study was carried out by Cavaleri et al. [26] adopting the Sargin concrete model [32]. More recently Parisi et al. [24] investigated the impact of different stress-strain models on $M-\chi$ curves. The results are compared to experimental $M-\chi$ diagrams from eccentric compression tests on

masonry specimens. Furthermore, their paper includes an incremental iterative procedure for the evaluation of moment-curvature relations in case of fixed eccentricity or constant axial load.

Strength and deformation assessment of a masonry sections under axial load and bending can be alternatively achieved using FEM software with fiber beam finite elements [33]. This approach is largely adopted for reinforced concrete and steel cross-sections.

Starting from the significant contributions of these past studies, the present paper tries to address the topic in an analytical way, providing a set of expressions useful for a direct calculation of $M-N$ and $M-\chi$ diagrams in a preliminary stage of assessment. Differently from the previous researches, the present work is focused on the derivation of closed-form equations both for strength domains and moment-curvature relationships.

In order to perform the calculation of the cross-section diagrams without the adoption of iterative procedures, the masonry stress-strain relationships assumed in the study are no-tension models with linear/bilinear behavior in compression. Particularly, the constitutive laws implemented in the calculations try to catch the experimental stress-strain behavior with an increasing representability: Elastic-Brittle (EB) model, Elastic-Plastic (EP) model, Elastic-Softening (ES) model.

2. Rectangular URM cross-section analysis

Cross-section geometry and masonry constitutive model are required for the evaluation of $M-N$ and $M-\chi$ diagrams. In the case of rectangular URM members without internal leaf, the geometry of the section is defined by height h and width B (Fig. 1a).

Uniaxial response of the material is represented by $\sigma_m-\varepsilon_m$ stress-strain diagram (Fig. 1b). Looking at experimental results [29,34], the following parameters can be defined: E_m is the initial Young modulus; f_m is the maximum compressive strength; f_r is the residual compressive strength; ε_{m1} is the peak axial strain; ε_{mu} is the ultimate axial strain. Once these parameters are extracted from laboratory test, the analytical constitutive model of masonry can be described with the expressions available in

technical guidelines and scientific literature. American standard ACI 530 [35] adopts elastic-perfectly-plastic model for URM having maximum strength f_m and constant value of $\epsilon_{mu} = 0.0035$ (clay bricks). Eurocode 6 [27], following the reinforced concrete guidelines, suggests a parabola-rectangle law with three input parameters (f_m , ϵ_{m1} , ϵ_{mu}). Starting from the concrete stress-strain model proposed by Kent and Park [36], more sophisticated relationships have been proposed accounting: linear strain softening [25]; effect of lime mortar joints [34]; probabilistic best fitting with respect to experimental test [29]. As reported in the introduction, in the present work three linear/bilinear stress-strain laws are adopted for the derivation of $M-N$ and $M-\chi$ closed-form expressions (Fig. 1c): Elastic-Brittle (EB), Elastic-Plastic (EP), Elastic-Softening (ES). Masonry tensile strength is assumed equal to zero according to international codes [27,35].

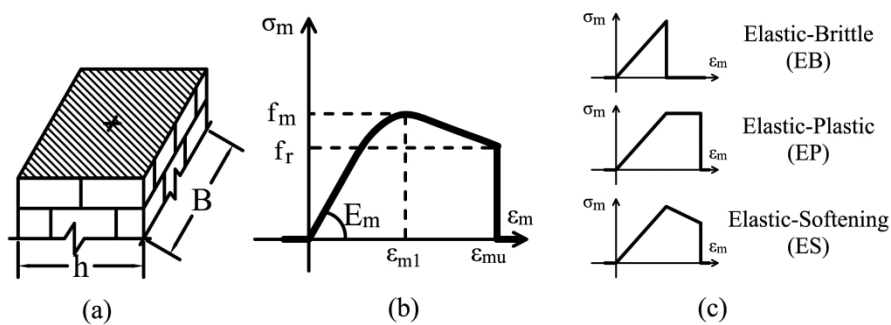


Fig. 1. (a) Geometry of the cross-section; (b) representative stress-strain diagram for masonry material; (c) constitutive models adopted in the study.

2.1. Elastic-Brittle Constitutive Law

The EB constitutive law is reported in Fig. 2a. The behavior in compression is elastic up to the strength limit f_m . The ultimate strain in compression ϵ_{mu} is equal to the axial strain at maximum ϵ_{m1} (brittle behavior).

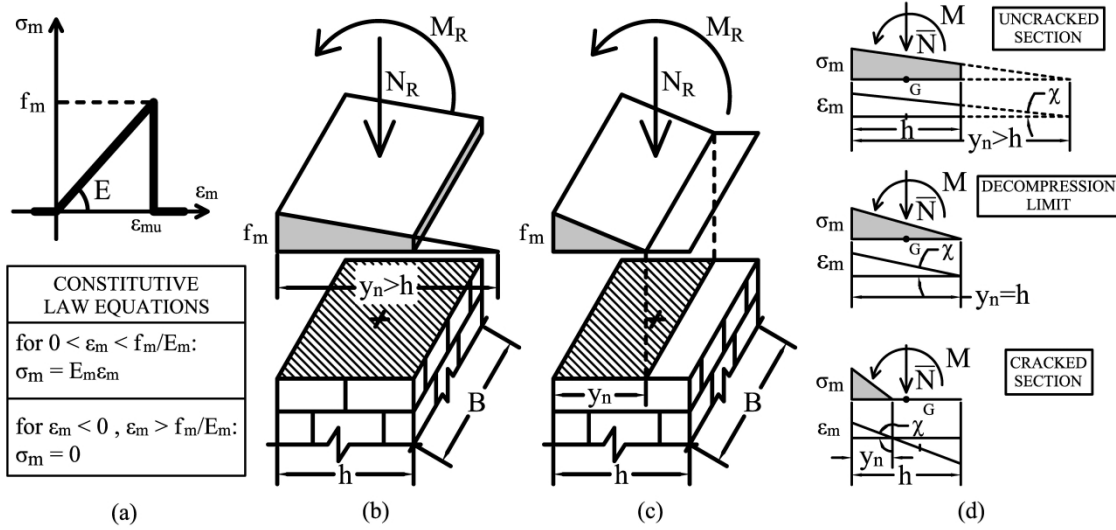


Fig. 2. (a) EB constitutive law; (b) ultimate limit state in uncracked condition; (c) ultimate limit state in cracked condition; (d) M - χ diagram stages.

2.1.1. M - N Interaction Diagram

The M - N diagram is evaluated by assuming the stress $\sigma_m = f_m$ at the extreme fiber of the section (Fig. 2b-c). From an analytical point of view, the interaction curve is defined by two branches. The first branch collects the ultimate points of the cross-section in cracked condition (Fig. 2c) and is defined for a resisting axial load N_R ranging from 0 to $N_{R,dec} = f_m B h / 2$, where $N_{R,dec}$ is the axial strength at the decompression limit of the cross-section. The second branch represents the resistance of the uncracked section and is defined from $N_R = N_{R,dec}$ to $N_R = N_{R,com}$, where $N_{R,com} = f_m B h$ is the maximum compressive strength of the cross-section. The following section reports the algebraic procedure adopted for the calculation of M - N diagrams. The results are summarized in Table 2.

- *Cracked section*: $0 \leq N_R \leq N_{R,dec}$

The analytical function $M_R = f(N_R)$ is derived solving a non-linear system in two equations (i.e. the axial equilibrium and rotational equilibrium) and two variables: the neutral axis depth y_n and the axial load N_R .

The axial and rotational equilibrium are reported in Eqs. (1) and (2) respectively:

$$N_R = \frac{1}{2} f_m B y_n \quad (1)$$

$$M_R = \frac{1}{2} f_m B y_n \left[\frac{h}{2} - \frac{y_n}{3} \right] \quad (2)$$

By extracting the neutral axis y_n from Eq. (1) and substituting in Eq. (2), the expression of the interaction diagram in cracked condition is defined by Eq. (3):

$$M_R = N_R \left[\frac{h}{2} - \frac{2N_R}{3f_m B} \right] \quad (3)$$

- *Uncracked section: $N_{R,dec} \leq N_R \leq N_{R,com}$*

The interaction domain in uncracked condition is described by a line having as extreme points the decompression limit ($y_n = h$) and the pure compression ($y_n = \infty$) situations. The coordinates of these points are reported in Eqs. (4) and (5), while Eq. (6) describes the resulting domain.

$$N_{R,dec} = \frac{1}{2} f_m B h \quad M_{R,dec} = \frac{1}{12} f_m B h^2 \quad (4)$$

$$N_{R,com} = f_m B h \quad M_{R,com} = 0 \quad (5)$$

$$M_R = -\frac{1}{6} h N_R + \frac{1}{6} f_m B h^2 \quad (6)$$

- *Decompression limit curve: $0 \leq N_{dec} \leq N_{R,dec}$*

In the case of URM cross-sections, it is interesting to evaluate the decompression limit curve that collects the M - N coordinates for $y_n = h$. The curve is defined in the range $0 \leq N_{dec} \leq N_{R,dec}$: once the $N_{R,dec}$ is exceeded, the failure of the cross-section occurs before the partialization. In Eq. (7) the relative formula is reported.

$$M_{dec} = \frac{N_{dec}}{6} h \quad (7)$$

	Cracked Section	Uncracked Section
Strength Domain Equations $M_R = f(N_R)$	$M_R = N_R \left[\frac{h}{2} - \frac{2N_R}{3f_m B} \right]$	$M_R = -\frac{1}{6}hN_R + \frac{1}{6}f_m Bh^2$
Decompression Limit	$M_{dec} = \frac{N_{dec}}{6}h$	-
Interval of Validity	$0 \leq N \leq N_{R,dec} = f_m Bh/2$	$N_{R,dec} \leq N \leq N_{R,com} = f_m Bh$

Table 2. EB constitutive law: strength domain.

2.1.2. M - χ Moment-Curvature Diagram

The evaluation of the moment-curvature (M - χ) diagram is performed for a given axial load \bar{N} (Fig. 2d). The curve is defined by two branches: the first one is related to the behavior in uncracked condition while the second one is referred to the cracked state. The decompression limit of the cross-section defines the boundary between the two parts (Table 3).

	Uncracked Section	Cracked Section
Moment-Curvature Equations $M = f(\chi)$	$M = EI\chi = \frac{1}{12}EBh^3\chi$	$M = \bar{N} \cdot \left(\frac{h}{2} - \sqrt{\frac{2\bar{N}}{9BE\chi}} \right)$
Interval of Validity	$0 \leq \chi \leq \chi_{dec} = 2\bar{N} / (EBh^2)$	$\chi_{dec} \leq \chi \leq \chi_u = f_m^2 B / (2E\bar{N})$

Table 3. EB constitutive law: moment-curvature equations.

- *Uncracked section:* $0 \leq \chi \leq \chi_{dec}$

The cross-section has elastic response until the decompression limit. The curvature at decompression limit is reported in Eq. (8):

$$\chi_{dec} = \epsilon_m/h = \sigma_m/(Eh) = 2\bar{N} / (EBh^2) \quad (8)$$

the corresponding moment-curvature analytical relation is reported in Eq. (9):

$$M = EI\chi = \frac{1}{12}EBh^3\chi \quad (9)$$

- *Cracked section*: $\chi_{dec} \leq \chi \leq \chi_u$

The curvature at ultimate limit is given in Eq. (10):

$$\chi_u = \varepsilon_{mu}/y_n = f_m^2 B/(2E \bar{N}) \quad (10)$$

The analytical equation of the non-linear branch is derived by extracting the variable y_n from the translational equilibrium equation, Eq. (11), and substituting it in the rotational one, Eq. (12):

$$\bar{N} = \frac{1}{2} \sigma_m B y_n = \frac{1}{2} \varepsilon_m E B y_n = \frac{1}{2} \chi E B y_n^2 \quad y_n = \sqrt{\frac{2\bar{N}}{BE\chi}} \quad (11)$$

$$M = \bar{N} \cdot \left(\frac{h}{2} - \sqrt{\frac{2\bar{N}}{9BE\chi}} \right) \quad (12)$$

2.1.3. 3D M-N- χ Diagram

A clear graphical representation of the flexural capacity of URM cross-sections can be provided by the 3D M-N- χ diagram. This envelope curve allows the visualization of the curvature ductility depending on the axial load insisting over the cross-section. As mentioned before, in case of EB model, the URM cross-section exhibits nonlinear deformations only for $N \leq N_{R,dec}$ (Ductile Curvature Region). Once the axial force at decompression $N_{R,dec}$ is exceeded, the section behaves in an elastic-brittle manner (Brittle Curvature Region). The 3D diagram of a representative cross-section is reported in Fig. 3. The geometrical and mechanical characteristics are: $B = 1$ m, $h = 1$ m, $E_m = 2000$ MPa, $f_m = 3$ MPa.

The maximum bending capacity of the section occurs in cracked condition for a level of normalized axial load $n = N/(f_m B h) = 0.37$. The curvature ductility, defined as the ratio between the ultimate curvature and the one at decompression χ_u/χ_{dec} , is larger than 20 for $n < 0.2$.

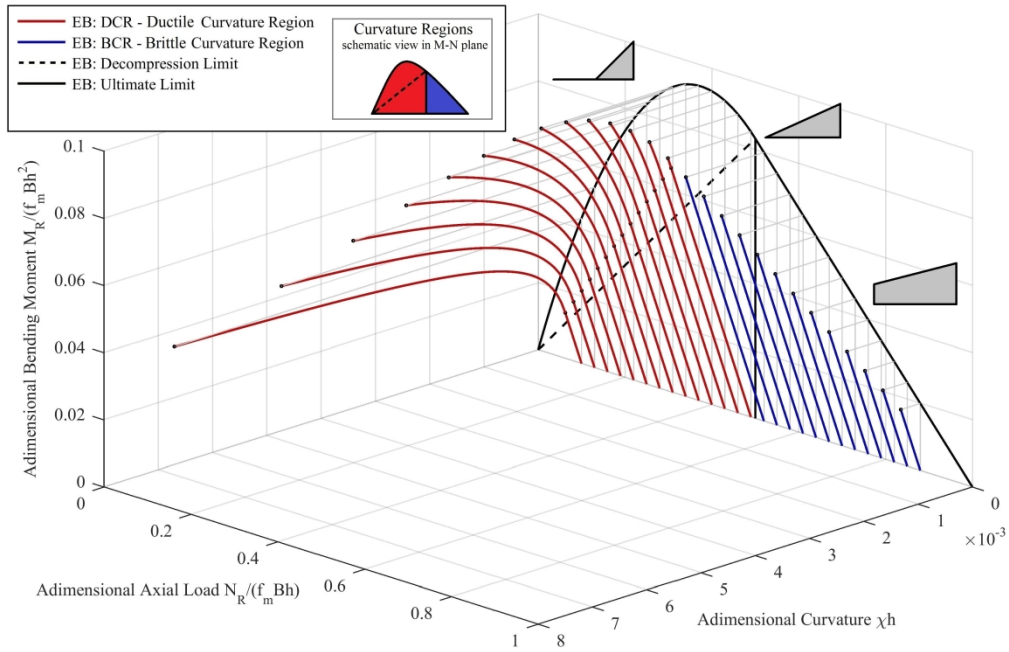


Fig. 3. 3D M-N- χ diagram for EB model.

2.2. Elastic-Plastic (EP) Constitutive Law

In order to take into account the redistribution of stresses inside the cross-section, international building codes [27,35] suggest the inclusion of a plastic plateau in the stress-strain relationship of masonry. In Fig. 4a, EP model is reported.

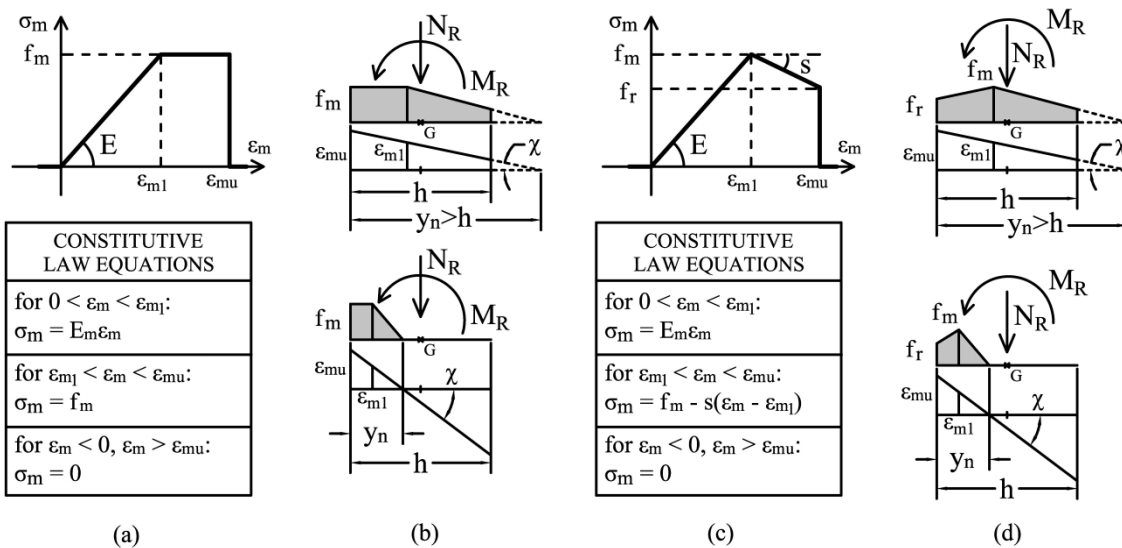


Figure 4. (a) EP constitutive law; (b) EP: ultimate limit state; (c) ES constitutive law; (d) ES: ultimate limit state.

2.2.1. M-N Interaction Diagram

Two limit domains can be evaluated for the case of EP masonry material: the elastic limit domain (identical to the EB ultimate limit domain) is defined by imposing $\varepsilon_m = \varepsilon_{m1}$ at the extreme fiber of the cross section; similarly, the ultimate limit domain is derived by imposing $\varepsilon_m = \varepsilon_{mu}$.

The ultimate limit domain is described by two branches. The first one is defined for $0 \leq N_R \leq N_{R,dec}$ where (Eq. (13)):

$$N_{R,dec} = f_m B h (1 - 0.5 \varepsilon_{m1}/\varepsilon_{mu}) \quad (13)$$

This interval collects the ultimate limit points in cracked condition. The second branch fits in the range $N_{R,dec} \leq N_R \leq N_{R,com} = f_m B h$ and includes the ultimate limit points in uncracked state.

Similarly, the decompression limit is defined in two ranges. The first one ranges in $0 \leq N_{dec} \leq f_m B h/2$ and collects the decompression limit points with $\varepsilon_m \leq \varepsilon_{m1}$ (equivalent to the decompression limit for EB model). The second one, defined for $f_m B h/2 \leq N_{dec} \leq N_{R,dec}$, includes the decompression limit point in elastoplastic condition. The analytical expressions of the *M-N* interaction diagrams are listed in Table 4.

	Cracked Section		Uncracked Section
Strength Domain Equations $M_R = f(N_R)$	$M_R = \frac{N_R}{2} h - \frac{2(\varepsilon_{m1}^2 - 3\varepsilon_{m1}\varepsilon_{mu} + 3\varepsilon_{mu}^2)}{3Bf_m(\varepsilon_{m1} - 2\varepsilon_{mu})^2} N_R^2$		$M_R = \left(\frac{1}{2} - \frac{1}{3} \frac{\varepsilon_{m1}}{\varepsilon_{mu}} \right) h [f_m B h - N_R]$
Decompression Limit	$M_{dec} = \frac{N_{dec}}{6} h$	$M_{dec} = \left(\frac{h}{2} + \frac{2(N_{dec} - f_m B h)}{3f_m B} \right) (f_m B h - N_{dec})$	-
Interval of Validity	$0 \leq N \leq f_m B h/2$	$f_m B h/2 \leq N \leq N_{R,dec} = f_m B h (1 - 0.5 \varepsilon_{m1}/\varepsilon_{mu})$	$N_{R,dec} \leq N \leq N_{R,com} = f_m B h$

Table 4. EP constitutive law: strength domain.

2.2.2. $M-\chi$ Moment-Curvature Diagram

Analytical equations of $M-\chi$ diagrams are derived for the three axial load intervals of validity reported in Table 4.

- High Ductility Curvature Region (HDCR)

Axial load range: $0 \leq \bar{N} \leq f_m B h / 2$

Description of the phenomena: Phase I. Elastic behavior of the cross-section up to the decompression limit, which occurs before the achievement of the elastic strain ε_{mI} ; Phase II. Achievement of the elastic strain ε_{mI} in cracked condition; Phase III. Achievement of the ultimate strain ε_{mu} in cracked condition.

- Moderate Ductility Curvature Region (MDCR)

Axial load range: $f_m B h / 2 \leq \bar{N} \leq f_m B h (1 - 0.5 \varepsilon_{mI} / \varepsilon_{mu})$

Description of the phenomena: Phase I. Elastic behavior of the cross-section up to the achievement of the elastic strain ε_{mI} ; Phase II. Elastoplastic response of the section up to decompression limit; Phase III. Elastoplastic behavior of the section in cracked condition up to the achievement of the ultimate strain ε_{mu} .

- Low Ductility Curvature Region (LDCR)

Axial load range: $f_m B h (1 - 0.5 \varepsilon_{mI} / \varepsilon_{mu}) \leq \bar{N} \leq f_m B h$

Description of the phenomena: Phase I. Elastic behavior of the cross section up to the achievement of the elastic strain ε_{mI} ; Phase II. Elastoplastic response of the section up to the ultimate strain ε_{mu} .

Equations and relevant intervals of validity of the three regions are listed in Table 5.

	HDCR	MDCR	LDCR
--	-------------	-------------	-------------

Axial Load	$0 < \bar{N} < \frac{1}{2} f_m B h$	$\frac{1}{2} f_m B h < \bar{N} < f_m B h \left(1 - \frac{1}{2} \frac{\varepsilon_{m1}}{\varepsilon_{mu}}\right)$	$f_m B h \left(1 - \frac{1}{2} \frac{\varepsilon_{m1}}{\varepsilon_{mu}}\right) < \bar{N} < f_m B h$
Phase I	$M = \frac{\chi}{EI} = 12 \frac{\chi}{EBh^3}$	$M = \frac{\chi}{EI} = 12 \frac{\chi}{EBh^3}$	$M = \frac{\chi}{EI} = 12 \frac{\chi}{EBh^3}$
	$0 \leq \chi \leq \chi_{dec} = 2 \bar{N} / (EBh^2)$	$0 \leq \chi \leq \chi_{m1} = 2(f_m B h - \bar{N}) / (EBh^2)$	$0 \leq \chi \leq \chi_{m1} = 2(f_m B h - \bar{N}) / (EBh^2)$
Phase II	$M = \bar{N} \cdot \left(\frac{h}{2} - \sqrt{\frac{2\bar{N}}{9BE\chi}} \right)$	$M = \frac{f_m B h^2}{2} - \frac{\bar{N}h}{2} - \frac{1}{3}(f_m B h - \bar{N}) \sqrt{\frac{2\varepsilon_{m1}}{\chi} \left(h - \frac{\bar{N}}{f_m B} \right)}$	$M = \frac{f_m B h^2}{2} - \frac{\bar{N}h}{2} - \frac{1}{3}(f_m B h - \bar{N}) \sqrt{\frac{2\varepsilon_{m1}}{\chi} \left(h - \frac{\bar{N}}{f_m B} \right)}$
	$\chi_{dec} \leq \chi \leq \chi_{m1} = f_m^2 B / (2E \bar{N})$	$\chi_{m1} \leq \chi \leq \chi_{dec} = \frac{f_m B \varepsilon_{m1}}{2(f_m B h - \bar{N})}$	$\chi_{m1} \leq \chi \leq \chi_{mu} = \frac{2\varepsilon_{mu}^2 (f_m B h - \bar{N})}{f_m B h^2 \varepsilon_{m1}}$
Phase III	$M = \frac{\bar{N}(f_m B h - \bar{N})}{2f_m B} - \frac{f_m B \varepsilon_{m1}^2}{24 \chi^2}$	$M = \frac{\bar{N}(f_m B h - \bar{N})}{2f_m B} - \frac{f_m B \varepsilon_{m1}^2}{24 \chi^2}$	-
	$\chi_{m1} \leq \chi \leq \chi_{mu} = \frac{f_m B \varepsilon_{mu} \left[1 - \frac{1}{2} \frac{\varepsilon_{m1}}{\varepsilon_{mu}} \right]}{\bar{N}}$	$\chi_{dec} \leq \chi \leq \chi_{mu} = \frac{f_m B \varepsilon_{mu} \left[1 - \frac{1}{2} \frac{\varepsilon_{m1}}{\varepsilon_{mu}} \right]}{\bar{N}}$	-

Table 5. EP constitutive law: moment-curvature equations.

2.2.3. 3D M - N - χ Diagram

The 3D M - N - χ diagram is reported in Fig. 5 for the representative cross-section defined in 2.1.3.

Here, $\varepsilon_{mu} = 0.0035$ is assumed as ultimate strain of masonry in compression. Given these parameters, the Ductility Curvature Regions are defined in the following intervals:

HDCR - $0 \leq n \leq 0.5$; MDCR - $0.5 \leq n \leq 0.785$; LDCR - $0.785 \leq n \leq 1$.

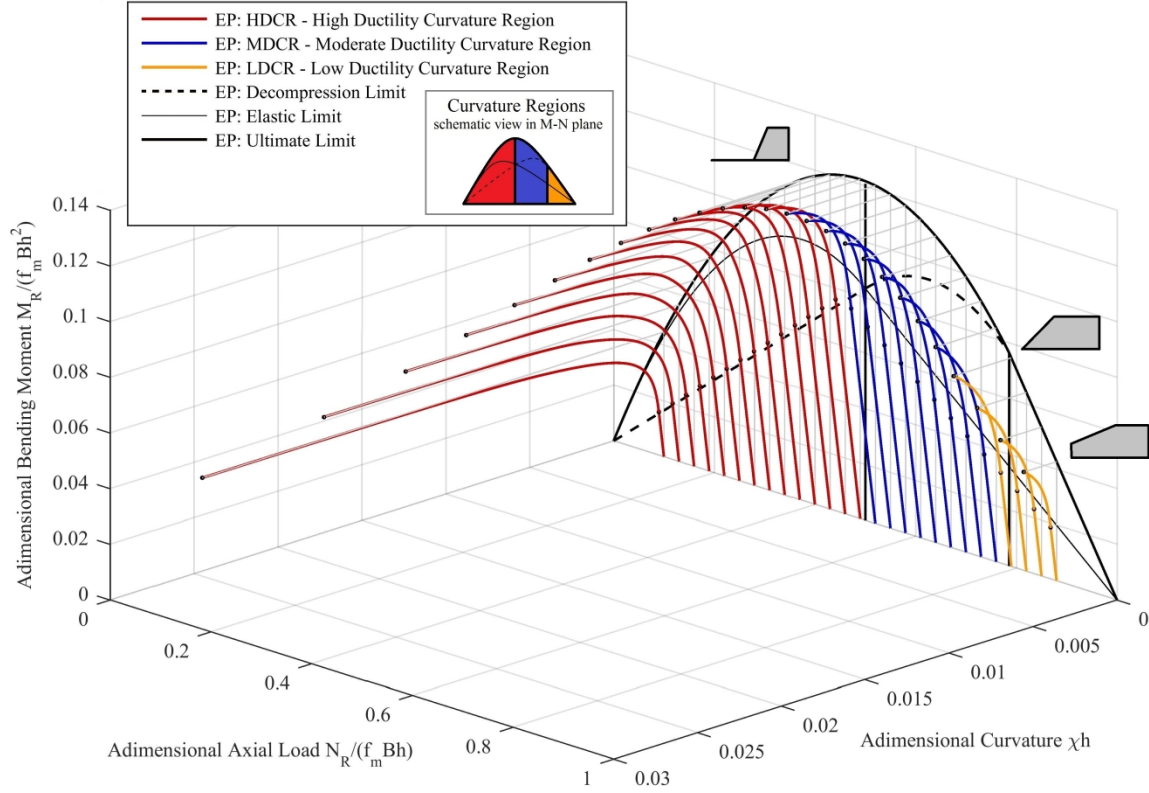


Figure 5. $M-N-\chi$ interaction diagram for EP constitutive model.

2.3. Elastic-Softening (ES) Constitutive Law

Constitutive laws with complex softening branch [24] are certainly the most suitable models for masonry material [7] and are usually adopted when the cross-section is discretized with fibers [3]. However, since advanced stress-strain relationships are defined by articulate equations, the closed-form integration of these models results in hardly manageable $M-N$ and $M-\chi$ expressions. For this reason, in the present work, the effect of the masonry strain softening is taken into account with a bilinear Elastic-Softening (ES) constitutive model.

The corresponding stress-strain curve is reported in Fig. 4b. The initial elastic branch is followed by a negative slope determined by the coefficient $s = (f_m - f_r) / (\epsilon_{mu} - \epsilon_{m1})$ where f_r is the residual strength at ultimate strain ϵ_{mu} .

2.3.1. M-N Interaction Diagram

The methodology adopted for EB and EP models is here extended to ES constitutive law. The two branches of the M-N interaction diagram, corresponding to cracked and uncracked conditions, join at the abscissa $N_R = N_{R,dec}$ (Eq. 14). Table 6 summarize the results.

$$N_{R,dec} = f_m Bh \left(1 - \frac{1}{2} \frac{\epsilon_{m1}}{\epsilon_{mu}} - \frac{1}{2} s \frac{(\epsilon_{mu} - \epsilon_{m1})^2}{f_m \epsilon_{mu}} \right) = \frac{1}{2} f_m Bh \left(1 + \frac{f_r}{f_m} \left(1 - \frac{\epsilon_{m1}}{\epsilon_{mu}} \right) \right) \quad (14)$$

		Cracked Section	
Strength			
Domain			
Equations			
$M_R = f(N_R)$			
Decompression			
Limit	$M_{dec} = \frac{N_{dec}}{6} h$		$M_{dec} = \frac{N_{dec} h}{2} - \frac{f_m Bh^2}{2} + \frac{1}{6} Bh^2 s (\epsilon_m - \epsilon_{m1}) \left(\frac{\epsilon_{m1} - 1}{\epsilon_m} \right)^2 - \frac{f_m Bh^2 \epsilon_{m1}}{2 \epsilon_m} \left(\frac{\epsilon_{m1} - 1}{3 \epsilon_m} - 1 \right)$ <p>where:</p> $\epsilon_m = \frac{f_m}{s} + \epsilon_{m1} - \frac{1}{Bhs} \left[N_{dec} + \frac{1}{2} \sqrt{4Bh(f_m + \epsilon_{m1}s)(f_m Bh - 2N_{dec}) + 4N_{dec}^2} \right]$
Interval of			
Validity	$0 \leq N_R \leq f_m Bh/2$		$f_m Bh/2 \leq N_R \leq \frac{1}{2} f_m Bh \left(1 + \frac{f_r}{f_m} \left(1 - \frac{\epsilon_{m1}}{\epsilon_{mu}} \right) \right)$
		Uncracked Section	
Strength			
Domain			
Equations			
$M_R = f(N_R)$			
Interval of			
Validity		$\frac{1}{2} f_m Bh \left(1 + \frac{f_r}{f_m} \left(1 - \frac{\epsilon_{m1}}{\epsilon_{mu}} \right) \right) \leq N_R \leq f_r Bh$	

Table 6. Elastic-Softening (ES) constitutive law: strength domain.

2.3.2. $M-\chi$ Moment-Curvature Diagram

Also in the case of ES material the $M-\chi$ diagram expressions are defined by means of three Ductility Curvature Regions.

- High Ductility Curvature Region (HDCR)

Axial load range: $0 \leq \bar{N} \leq f_m B h / 2$

Description of the phenomena: Phase I. Elastic behavior of the cross section up to decompression limit, which occurs before the achievement of the elastic strain ε_{m1} ; Phase II. Achievement of the elastic strain ε_{m1} in cracked condition; Phase III. Achievement of the maximum bending capacity; Phase IV: Decrease of the bending moment up to the achievement of the ultimate strain ε_{mu} in cracked condition.

- Moderate Ductility Curvature Region (MDCR)

Axial load range: $f_m B h / 2 \leq \bar{N} \leq \frac{1}{2} f_m B h \left(1 + \frac{f_r}{f_m} \left(1 - \frac{\varepsilon_{m1}}{\varepsilon_{mu}} \right) \right)$

Description of the phenomena: Phase I. Elastic behavior of the cross section up to the achievement of the elastic strain ε_{m1} ; Phase II. Elastoplastic response of the section up to decompression limit; Phase III. Achievement of the maximum bending capacity in cracked condition; Phase IV: Decrease of the bending moment up to the achievement of the ultimate strain ε_{mu} .

- Low Ductility Curvature Region (LDCR)

Axial load range: $\frac{1}{2} f_m B h \left(1 + \frac{f_r}{f_m} \left(1 - \frac{\varepsilon_{m1}}{\varepsilon_{mu}} \right) \right) \leq \bar{N} \leq f_m B h$

Description of the phenomena: Phase I. Elastic behavior of the cross section up to the achievement of the elastic strain ε_{m1} ; Phase II. Achievement of the maximum bending capacity; Phase III: Decrease of the bending moment up to the achievement of the ultimate strain ε_{mu} in uncracked condition.

All the relevant equations are reported in Table 7.

	HDCR
Axial Load	$0 < \bar{N} < \frac{1}{2} f_m B h$
Phase I	$M = \frac{\chi}{EI} = 12 \frac{\chi}{EBh^3}, \quad \text{for: } 0 \leq \chi \leq \chi_{dec} = 2 \bar{N} / (EBh^2)$
Phase II	$M = \bar{N} \cdot \left(\frac{h}{2} - \sqrt{\frac{2\bar{N}}{9BE\chi}} \right), \quad \text{for: } \chi_{dec} \leq \chi \leq \chi_{m1} = f_m^2 B / (2E \bar{N})$
Phase III	$M = \frac{\bar{N}h}{2} - \frac{f_m B y_n^2}{2} + \frac{B\chi s}{6} \left(y_n - \frac{\epsilon_{m1}}{\chi} \right)^3 + \frac{f_m B \epsilon_{m1}}{2\chi} \left(y_n - \frac{\epsilon_{m1}}{3\chi} \right)$
Phase IV	<p>where: $y_n = \frac{f_m + \epsilon_{m1}s}{\chi s} - \sqrt{\frac{f_m}{\chi^2 s^2} (f_m + \epsilon_{m1}s) - \frac{2\bar{N}}{B\chi s}},$</p> <p>for: $\chi_{m1} \leq \chi \leq \chi_{mu} = \frac{f_m B \epsilon_{mu} \left[1 - \frac{f_r}{f_m} \left(\frac{\epsilon_{m1}}{\epsilon_{mu}} - 1 \right) \right]}{2\bar{N}}$</p>
	MDCR
Axial Load	$\frac{1}{2} f_m B h < \bar{N} < \frac{1}{2} f_m B h \left(1 + \frac{f_r}{f_m} \left(1 - \frac{\epsilon_{m1}}{\epsilon_{mu}} \right) \right)$
Phase I	$M = \frac{\chi}{EI} = 12 \frac{\chi}{EBh^3}, \quad \text{for: } 0 \leq \chi \leq \chi_{m1} = 2(f_m B h - \bar{N}) / (EBh^2)$
Phase II	$M = \frac{\bar{N}h}{2} - \frac{f_m B h^2}{2} + \frac{1}{2} f_m B \left(1 - \frac{\chi(y_n - h)}{\epsilon_{m1}} \right) \left(h - y_n + \frac{\epsilon_{m1}}{\chi} \right) \left(\frac{y_n}{3} + \frac{2h}{3} - \frac{\epsilon_{m1}}{3\chi} \right) - \frac{1}{6} B s \left(y_n - \frac{\epsilon_{m1}}{\chi} \right)^2 (\epsilon_{m1} - y_n \chi)$ <p>where:</p> $y_n = \frac{f_m B \epsilon_{m1} + B \epsilon_{m1}^2 s + f_m B h \chi - \sqrt{B \chi (2f_m^2 B h - f_m B h^2 s \chi + 2f_m B h \epsilon_{m1} s - 2f_m \bar{N} - 2\bar{N} \epsilon_{m1} s)}}{B \chi (f_m + s \epsilon_{m1})}$ <p>for: $\chi_{m1} \leq \chi \leq \chi_{dec} = \frac{f_m + \epsilon_{m1}s}{hs} - \frac{1}{Bsh^2} \left[\bar{N} + \frac{1}{2} \sqrt{4Bh(f_m + \epsilon_{m1}s)(f_m B h - 2\bar{N}) + 4\bar{N}} \right]$</p>
Phase III	$M = \frac{\bar{N}h}{2} - \frac{f_m B y_n^2}{2} + \frac{B\chi s}{6} \left(y_n - \frac{\epsilon_{m1}}{\chi} \right)^3 + \frac{f_m B \epsilon_{m1}}{2\chi} \left(y_n - \frac{\epsilon_{m1}}{3\chi} \right)$
Phase IV	

	<p>where: $y_n = \frac{f_m + \varepsilon_{m1}s}{\chi s} - \sqrt{\frac{f_m}{\chi^2 s^2} (f_m + \varepsilon_{m1}s) - \frac{2\bar{N}}{B\chi s}}$,</p> <p>for: $\chi_{m1} \leq \chi \leq \chi_{mu} = \frac{f_m B \varepsilon_{mu} \left[1 - \frac{f_r}{f_m} \left(\frac{\varepsilon_{m1}}{\varepsilon_{mu}} - 1 \right) \right]}{2\bar{N}}$</p>
	LDCR
Axial Load	$f_m B h \left(1 - \frac{1}{2} \frac{\varepsilon_{m1}}{\varepsilon_{mu}} \right) < \bar{N} < f_m B h$
Phase I	$M = \frac{\chi}{EI} = 12 \frac{\chi}{EBh^3}$, for: $0 \leq \chi \leq \chi_{m1} = 2(f_m B h - \bar{N}) / (EBh^2)$
Phase II	$M = \frac{\bar{N}h}{2} - \frac{f_m B h^2}{2} + \frac{1}{2} f_m B \left(1 - \frac{\chi(y_n - h)}{\varepsilon_{m1}} \right) \left(h - y_n + \frac{\varepsilon_{m1}}{\chi} \right) \left(\frac{y_n}{3} + \frac{2h}{3} - \frac{\varepsilon_{m1}}{3\chi} \right) - \frac{1}{6} B s \left(y_n - \frac{\varepsilon_{m1}}{\chi} \right)^2 (\varepsilon_{m1} - y_n \chi)$ <p>where:</p>
Phase III	$y_n = \frac{f_m B \varepsilon_{m1} + B \varepsilon_{m1}^2 s + f_m B h \chi - \sqrt{B \chi (2f_m^2 B h - f_m B h^2 s \chi + 2f_m B h \varepsilon_{m1} s - 2f_m \bar{N} - 2\bar{N} \varepsilon_{m1} s)}}{B \chi (f_m + s \varepsilon_{m1})}$ <p>for: $\chi_{m1} \leq \chi \leq \chi_{mu} = \frac{\varepsilon_{mu}}{h} - \frac{\bar{N} \varepsilon_{m1}}{f_m B h^2} + \frac{\varepsilon_{m1}^2}{f_m B h^2} \sqrt{f_m B^2 h^2 (2\varepsilon_{m1} \varepsilon_{mu} s - \varepsilon_{m1} s - f_m \varepsilon_{m1} - \varepsilon_{mu}^2 s + 2f_m \varepsilon_{mu}) + \bar{N} (\bar{N} \varepsilon_{m1} - 2f_m B h \varepsilon_{mu})}$</p>

Table 7. Elastic-Softening (ES) constitutive law: moment-curvature equations.

2.3.3. 3D M-N- χ Diagram

In Fig. 6, the 3D M-N- χ diagram is reported for the representative cross-section. The residual strength is assumed as $f_r = 0.8f_m$, according to Augenti et al. [23]. The resulting Ductility Curvature Regions are: HDCR - $0 \leq n \leq 0.5$; MDCR - $0.5 \leq n \leq 0.729$; LDCR - $0.729 \leq n \leq 1$.

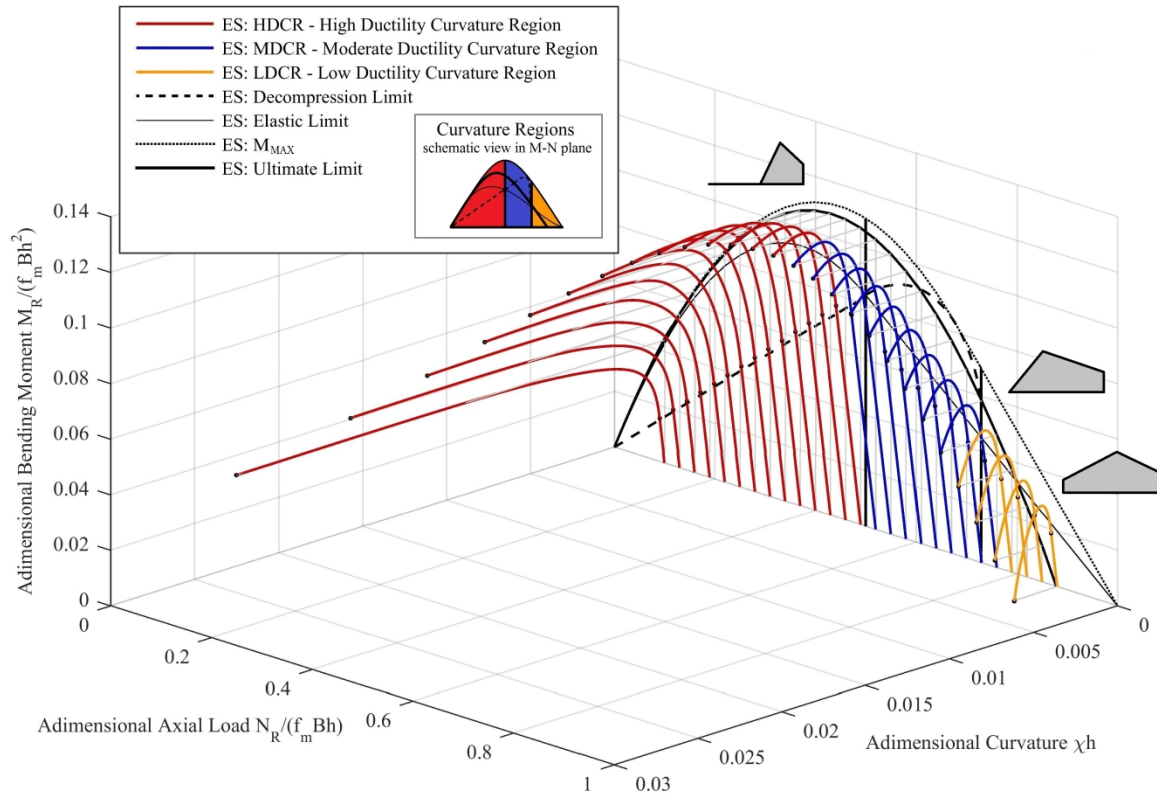


Figure 6. M-N- χ interaction diagram for ES constitutive model.

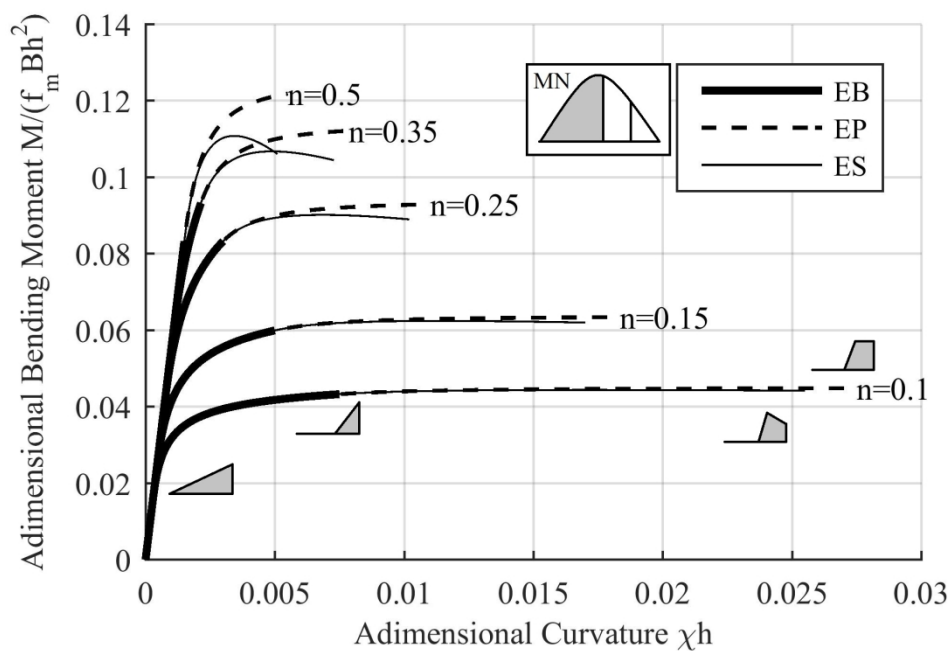
2.4. Discussion of the results

The representative M - χ diagrams for the three stress-strain constitutive models (EB, EP, ES) are collected in Fig. 7. Different levels of normalized axial load n are considered.

In Fig. 7a, the M - χ behavior in HDCR is reported. For any value of n , the EB model provide conservative results both in terms of bending resistance (M_R) and ultimate curvature (χ_u); for levels of $n < 0.15$ the percentage error in the evaluation of the maximum carrying capacity of the section is lower than 5% compared to the most accurate ES model. Similar conclusion affects the comparison between the EP and ES model. The adoption of a perfectly-plastic plateau is reasonable for value of n up to 0.25. In the extreme case of $n = 0.5$, the comparison in terms of ultimate curvatures is still acceptable but the difference in maximum bending capacity is greater than 10%.

Fig. 7b reports the results comparison in MDCR. In this region, EB model behaves linearly since it cannot redistribute stresses over the height of the cross-section, resulting in a conservative estimation of M_R and χ_{mu} . Comparing EP and ES models, the difference in ultimate bending moment increase up to 20%.

Finally, in the LDCR (Fig. 7c), strong differences between the three constitutive models are detected. For a level of $n = 0.8$, the EB model provide a M_R which is 50% lower than the maximum resisting moment of the ES constitutive law. For the same value of n , the percentage difference in maximum moment between EP and ES is greater than 28%. Strong level of axial compression ($n = 0.9$) accentuates the differences described before: the difference between EP and ES in terms of maximum bending moment is over 35% while the corresponding difference in terms of curvature reaches about 60%.



(a)

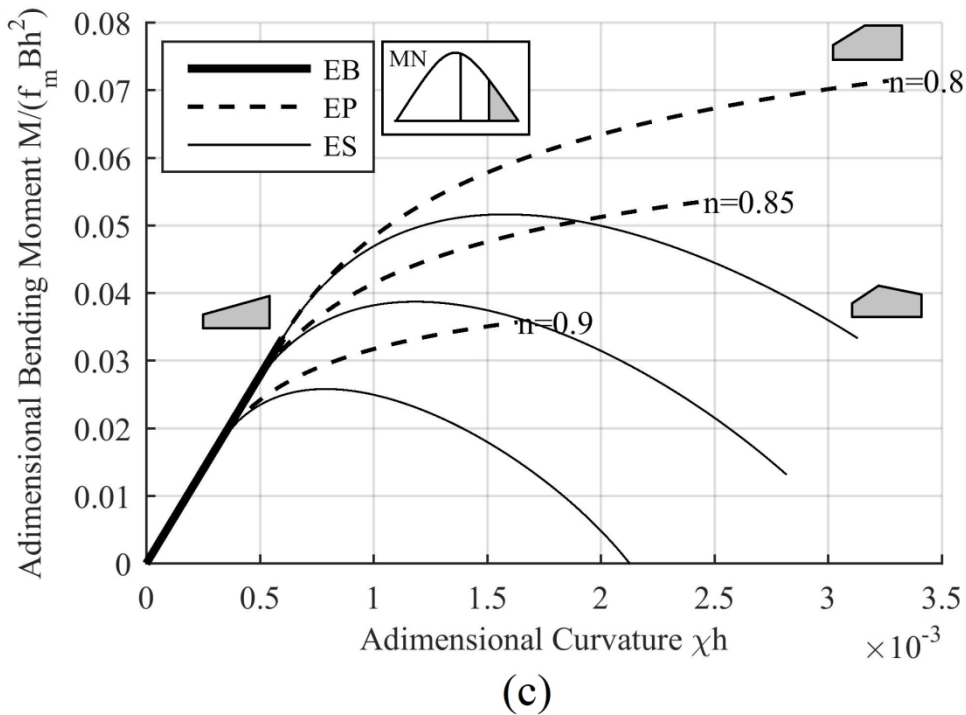
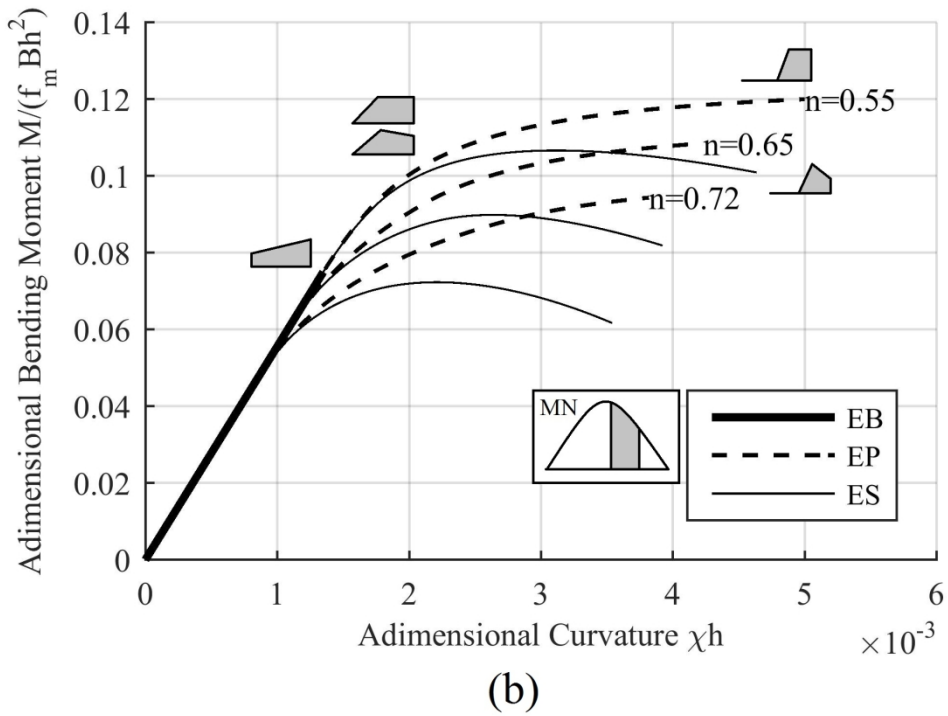


Figure 7. M - χ diagrams for different constitutive models. (a) HDCR: High Ductility Curvature Region; (b) MDCR: Moderate Ductility Curvature Region; (c) LDCR: Low Ductility Curvature Region.

3. Applications of M-N and M- χ expressions for non-linear structural analysis

As stated in the Introduction, cross-section representative diagrams are handy and understandable tools for practitioners involved in the structural assessment of URM buildings. Particularly, $M-N$ domains can be adopted for the safety verification of masonry members at the cross-section level. On the other side, $M-\chi$ relations can be assigned to beam-elements for nonlinear FEM analyses of URM structures in bending behavior.

The present Section addresses the second of the aforementioned applications. In order to simulate the experimental out-of-plane response of a stone masonry wall (Ferreira et al. [37]), nonlinear pushover analyses have been implemented by using different types of beam finite elements: beam-elements with $M-\chi$ nonlinearities and beam-elements with fiber discretization over the cross-section. In details, moment-curvature relationships have been evaluated via closed-form expressions for EB, EP and ES constitutive laws. Stress-strain models for fibers have been selected from literature studies: Kent and Park concrete model extended by Brencich et al. for the case of masonry [25]; Mander concrete model adopted by Raka et al. [38] and by Günay et al. [3] for URM piers.

3.1. Experimental benchmark and input data for pushover analyses

The experimental campaign conducted by Ferreira et al. [37] includes the top-displacement controlled out-of-plane loading of three stone masonry walls (Fig. 8) subjected to different levels of vertical load: $Test_1 - N_1 = 0 \text{ kN}$, $Test_2 - N_2 = 52 \text{ kN}$, $Test_3 - N_3 = 140 \text{ kN}$.

The geometrical characteristics of the specimens are: height of the wall $L = 2.50 \text{ m}$, depth and width of the rectangular cross-section respectively $h = 0.65$ and $B = 1.30 \text{ m}$. The unit weight of the masonry assemblage is $\gamma = 21 \text{ kN/m}^3$. The elastic properties of the material have been evaluated thanks to a vibration test, resulting in a value of the Young Modulus $E = 490 \text{ MPa}$.

The maximum horizontal displacement Δ_{max} imposed at the top of the wall is 17 cm ($Test_1$) and 20 cm ($Test_2$, $Test_3$).

In absence of a specific laboratory test on the URM assemblage of the walls, the following assumptions have been considered for the implementation of the pushover analyses. The strength of the masonry in compression (f_m) is assumed equal to 0.35 times the resistance of the units [39] i.e. $f_m = 0.35 \times 43.83 \approx 15$ MPa. This value agrees with tests on masonry prisms having the same typology of mortar and stone blocks (Vasconcelos [40]). The strain ductility of the material is assumed as $\mu = \varepsilon_{mu}/\varepsilon_{ml} = 2$, according to Kaushik et al. [34]. The residual strength is supposed equal to $f_r = 0.8f_m$ (Augenti et al. [23]).

3.2. Pushover analyses with M - χ nonlinearities

The numerical simulations of the tests have been performed in the *OpenSees* framework [41] implementing a displacement controlled pushover analysis. The wall is discretized by using 7 nonlinear beam finite elements. P-Delta effects are included in the calculation.

Flexural nonlinearity has been assigned in the form of M - χ relationships. M - χ curves for the three constitutive models (EB, EP, ES) were calculated using the equations reported in Tables 3, 5, 7. The normalized axial forces at the base of the wall for the three vertical load conditions are $n_1 = 0.0035$, $n_2 = 0.0076$, $n_3 = 0.0145$. It is important to observe that these low axial loads generate overlapped moment-curvature diagrams for EB, EP and ES constitutive models. As discussed in 2.4. (Fig. 7a., $n < 0.1$) the difference between the three laws is appreciated only in terms of ultimate curvature χ_u . The comparisons between experimental tests and numerical outcomes are reported in Fig. 9. For the three levels of axial load, the finite element models provide good results in terms of peak base shear capacity and residual force after peak. Percentage errors between numerical results and experimental data are reported in Table 8. As expected, given the similarity of M - χ curves from EB-EP-ES models, the pushover diagrams result analogous for the three material constitutive laws. In terms of deformations, the maximum curvature reached at the base of the wall is lower than the ultimate value

χ_u for EB-EP-ES models: in other words, the toe compression failure is never achieved. This numerical result is in agreement with the experimental test observations reported in [37].

	Test_1		Test_2		Test_3	
	$V_{B,P}$	$V_{B,R}$	$V_{B,P}$	$V_{B,R}$	$V_{B,P}$	$V_{B,R}$
M-χ Nonlinearity (EB-EP-ES)	17.44	5.16	22.46	8.44	19.47	15.23
Fiber (Brencich, 2009)	14.57	8.03	19.40	2.41	16.81	6.89
Fiber (Raka, 2015)	10.00	7.67	18.75	2.63	16.27	6.47
$V_{B,P}$: Peak base shear						
$V_{B,R}$: Residual base shear after peak						

Table 8. Percentage errors between numerical outcomes and experimental results.

3.3. Pushover analyses with fiber beam-elements

In order to assess the accuracy of the pushover analyses with $M-\chi$ nonlinearities, two finite element models with fiber subdivision over the cross-section have been implemented. The first one assumes the no-tension stress-strain constitutive law initially proposed by Kent and Park for concrete material [36] and readopted by Brencich et al. [25] for the case of masonry. The second model consider the concrete compressive stress-strain relationship proposed by Mander et al. [42] with tensile strength characterized by exponential decay. Also this model has been previously used for the analysis of URM members by Raka et al. [38] and by Günay et al. [3].

Table 8 reports the percentage errors of the two numerical simulations respect to experimental data. It can be observed that the results discrepancies between the two models are limited. Maximum differences are detected in the peak base shear ($V_{B,P}$) for *Test_1* (10.00% Raka vs. 14.57% Brencich). Fiber models and $M-\chi$ models displays comparable percentage errors respect to experimental data.

Particularly, fiber models slightly overestimate the residual base shear capacity for *Test_1* and *Test_2* while the analyses performed with $M-\chi$ nonlinearities provide conservative results for the three values of the investigated axial loads.

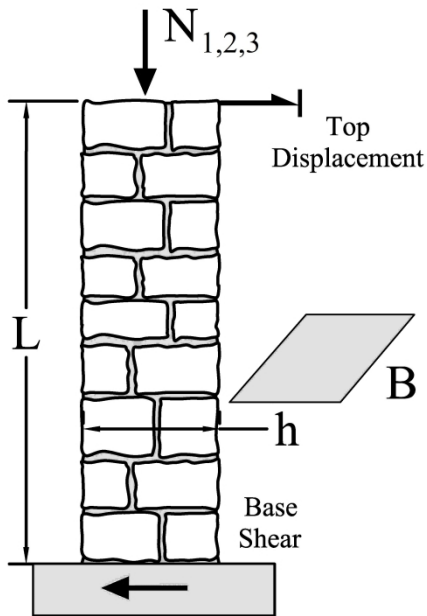


Fig. 8. Test setup of the experimental campaign conducted by Ferreira et al. [29]

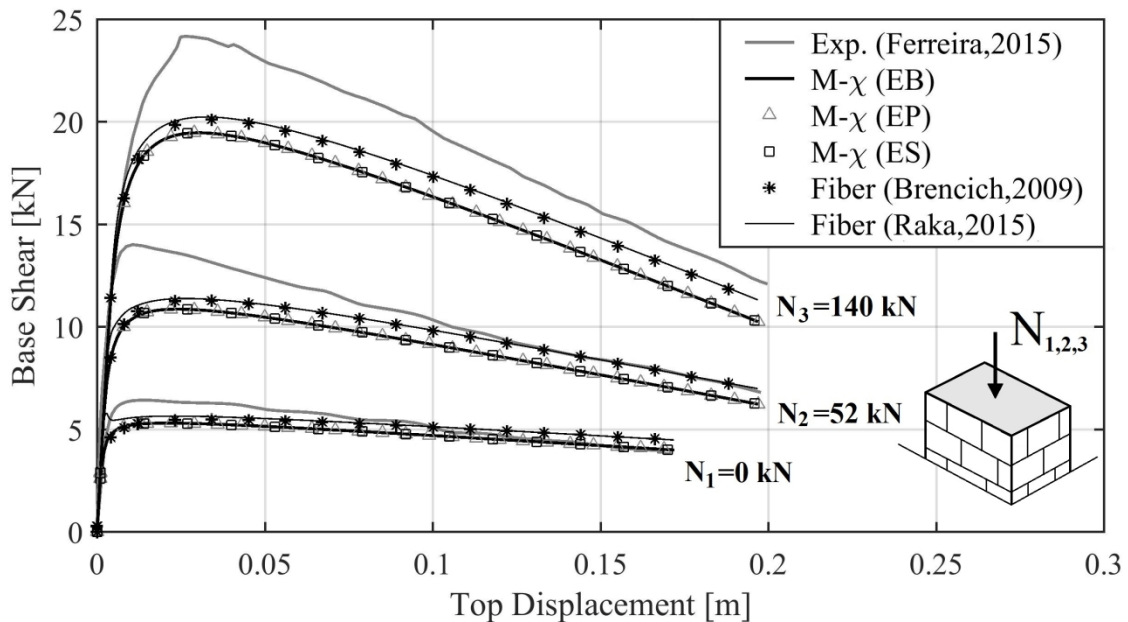


Fig. 9. Comparison between experimental results (Ferreira et al.) and numerical analyses based on the $M-\chi$ nonlinearities and fibers cross-section subdivision.

4. Conclusions

In the present paper, the flexural strength-ductility assessment of URM rectangular cross-sections has been presented via closed-form expressions. Three simplified stress-strain constitutive models have been considered for the representation of the stress-strain behavior of masonry: Elastic-Brittle (EB), Elastic-Plastic (EP) and Elastic-Softening (ES) laws.

Analytical closed-form equations have been derived and tested on a representative URM section. It can be observed that the outcomes are in agreement with the results presented in previous studies [23–25,43]:

- (i) EB constitutive law provides conservative results both in terms of flexural capacity and ultimate curvature. Obviously, when the normalized axial load n exceeds 0.5, the results of this model are inaccurate because the stress redistribution over the cross-section is not reproduced.
- (ii) EP model generates three Ductility Curvature Regions (DCR): High, Moderate and Low DCR. In HDCR the $M-\chi$ response is almost elastic-perfectly-plastic. On the contrary, MDCR and LDCR are characterized by hardening-type $M-\chi$ backbone curves.
- (iii) ES stress-strain relationship defines three Ductility Curvature Regions. Particularly, as confirmed by past studies [23], the influence of the strain softening is more relevant when increasing the applied axial force. For $n > 0.5$, the $M-\chi$ diagram is characterized by a sloping branch after peak that means unstable behavior of the masonry element for increasing lateral loads. On the contrary, when $n < 0.35$, the difference between ES and EP laws is limited.

The last part of the paper investigates the applicability of the closed-form expressions for the numerical assessment of masonry elements under transversal forces. As regard, it is specified that a seismic analysis based on a purely bending response is valid only for masonry columns and slender walls, usually not affected by shear damages.

The results of out-of-plane experimental tests on masonry walls [37] have been used as benchmark. Two sorts of nonlinear finite element analyses have been implemented to reproduce the laboratory tests. The first type adopts beam-elements with $M-\chi$ nonlinearities derived from closed-form expressions. The second one includes beam-elements with fiber discretization over the cross-section. Advanced masonry stress-strain constitutive laws have been assigned to fibers, as suggested by previous research investigations [25,38].

The comparison between experimental data and numerical outcomes shows that the models with $M-\chi$ nonlinearities provide good results in terms of peak base shear capacity and residual force after peak. Furthermore, the results are conservative for the investigated scenarios. As expected, due to the low axial load acting on the wall, EB, EP and ES models provide overlapped force-displacement curves. Similar results are obtained from fiber models, proving the validity of $M-\chi$ approach for the analyzed cases. Maximum percentage error discrepancy between fiber and $M-\chi$ models does not exceed 9%. In conclusion, the proposed sets of $M-N-\chi$ closed-form expressions seem suitable for the flexural strength and ductility evaluation of URM rectangular cross-sections. Furthermore, the numerical results suggest that it is possible to provide a relatively fast estimation of the out-of-plane behavior of a masonry wall by implementing the $M-\chi$ closed-form expressions in beam finite element models.

References

- [1] Brandonisio G, Lucibello G, Mele E, Luca A De. Damage and performance evaluation of masonry churches in the 2009 L'Aquila earthquake. *Eng Fail Anal* 2013;34:693–714. doi:10.1016/j.engfailanal.2013.01.021.
- [2] Milani G. Lesson learned after the Emilia-Romagna, Italy, 20-29 May 2012 earthquakes: A limit analysis insight on three masonry churches. *Eng Fail Anal* 2013;34:761–78. doi:10.1016/j.engfailanal.2013.01.001.
- [3] Günay S, Giordano N, Takhirov S, Mosalam KM. Seismic response of a historical unreinforced masonry building damaged in the 2014 South Napa Earthquake. *Proc 16th World Conf Earthq Eng* 2017;4340.
- [4] Augenti N, Parisi F, Acconcia E. MADA: Online experimental database for mechanical modelling of existing masonry assemblages. *Proc 15th World Conf Earthq Eng* 2012.
- [5] Roca P, Cervera M, Gariup G, Pelà L. Structural analysis of masonry historical constructions. Classical and advanced approaches. *Arch Comput Methods Eng* 2010;17:299–325. doi:10.1007/s11831-010-9046-1.
- [6] Mendes N, Costa AA, Lourenço PB, Bento R, Felice G De, Gams M, et al. Methods and Approaches for Blind Test Predictions of Out-of-Plane Behavior of Masonry Walls : A Numerical Comparative Study Methods and Approaches for Blind Test Predictions of Out-of-Plane Behavior of Masonry Walls : A Numerical Comparative Study. *Int J Archit Herit* 2017;11:59–71. doi:10.1080/15583058.2016.1238974.
- [7] Lourenço PB. Computations on historic masonry structures. *Prog Struct Engng Mater* 2002;4:301–19. doi:10.1002/pse.120.
- [8] Lourenço PB, Mendes N, Marques R. Earthquake Design and Assessment of Masonry Structures: Review and Applications. *Trends Civ. Struct. Eng. Comput.*, Stirlingshire: Saxe-Coburg Publications; 2009, p. 77–101. doi:10.4203/csets.22.4.
- [9] Franchi A, Crespi P, Ronca P, Giordano N, Ransenigo G. In-situ tests , analytical and numerical studies for the assessment capacity of a historic building in l ' Aquila. XIII Int. Forum Le Vie dei Merc., Aversa - Capri, Italy: n.d.
- [10] Cascante G, Najjaran H, Crespi P. Novel Methodology for Nondestructive Evaluation of Brick Walls: Fuzzy Logic Analysis of MASW Tests. *J Infrastruct Syst* 2008;14:117–28. doi:10.1061/(ASCE)1076-0342(2008)14:2(117).
- [11] Crespi P, Franchi A, Ronca P, Giordano N, Scamardo M, Gusmeroli G, et al. From BIM to FEM: the analysis of an historical masonry building. *WIT Trans Built Environ* 2015;149:581–

92. doi:10.2495/BIM150471.

- [12] Lagomarsino S, Penna A, Galasco A, Cattari S. TREMURI program: An equivalent frame model for the nonlinear seismic analysis of masonry buildings. *Eng Struct* 2013;56:1787–99. doi:10.1016/j.engstruct.2013.08.002.
- [13] Lemos J V. Discrete Element Modeling of Masonry Structures. *Int J Archit Herit* 2007;1:190–213. doi:10.1080/15583050601176868.
- [14] Giordano A, Mele E, De Luca A. Modelling of historical masonry structures: Comparison of different approaches through a case study. *Eng Struct* 2002;24:1057–69. doi:10.1016/S0141-0296(02)00033-0.
- [15] Dejong MJ. Seismic Assessment Strategies for Masonry Structures. MASSACHUSETTS INSTITUTE OF TECHNOLOGY, 2009.
- [16] Crespi P, Franchi A, Giordano N, Scamardo M, Ronca P. Structural analysis of stone masonry columns of the Basilica S. Maria di Collemaggio. *Eng Struct* 2016;129. doi:10.1016/j.engstruct.2016.05.045.
- [17] Wilding BV, Beyer K. Force-displacement response of in-plane loaded unreinforced brick masonry walls: the Critical Diagonal Crack model. *Bull Earthq Eng* 2016;1–44. doi:10.1007/s10518-016-0049-7.
- [18] Tomaževič M. Shear resistance of masonry walls and Eurocode 6: shear versus tensile strength of masonry. *Mater Struct* 2009;42:889–907. doi:10.1617/s11527-008-9430-6.
- [19] Frisch-Fay R. Stability of masonry piers. *Int J Solids Struct* 1975;11:187–98. doi:10.1016/0020-7683(75)90052-9.
- [20] Tomaževič M. Dynamic modelling of masonry buildings: Storey mechanism model as a simple alternative. *Earthq Eng Struct Dyn* 1987;15:731–49. doi:10.1002/eqe.4290150606.
- [21] La Mendola L, Papia M, Zingone G. Stability of Masonry Walls Subjected to Seismic Transverse Forces. *J Struct Eng* 1995;121:1581–7. doi:10.1061/(ASCE)0733-9445(1995)121:11(1581).
- [22] Gurel MA, Pekgokgoz RK, Cili F. Strength capacity of unreinforced masonry cylindrical columns under seismic transverse forces. *Bull Earthq Eng* 2012;10:587–613. doi:10.1007/s10518-011-9297-8.
- [23] Parisi F, Augenti N. Assessment of unreinforced masonry cross sections under eccentric compression accounting for strain softening. *Constr Build Mater* 2013;41:654–64. doi:10.1016/j.conbuildmat.2012.12.039.
- [24] Parisi F, Sabella G, Augenti N. Constitutive model selection for unreinforced masonry cross sections based on best-fit analytical moment-curvature diagrams. *Eng Struct* 2016;111:451–

66. doi:10.1016/j.engstruct.2015.12.036.

- [25] Brencich A, Felice G de. Brickwork under eccentric compression: Experimental results and macroscopic models. *Constr Build Mater* 2009;23:1935–46.
doi:10.1016/j.conbuildmat.2008.09.004.
- [26] Cavaleri L, Failla A, La Mendola L, Papia M. Experimental and analytical response of masonry elements under eccentric vertical loads. *Eng Struct* 2005;27:1175–84.
doi:10.1016/j.engstruct.2005.02.012.
- [27] Comité Européen de Normalisation. EN 1996-1-1:2005. Eurocode 6: design of masonry structures – Part 1–1: General rules for reinforced and unreinforced masonry structures. Brussels: 2005.
- [28] Turnsek V, Cacovic F. Some experimental results on the Strength of Brick Masonry Walls. *Proc 2nd Int Brick Mason Conf* 1971.
- [29] Augenti N, Parisi F. Constitutive Models for Tuff Masonry under Uniaxial Compression. *J Mater Civ Eng* 2010;22:1102–11. doi:10.1061/(ASCE)MT.1943-5533.0000119.
- [30] La Mendola L. Influence of nonlinear constitutive law on masonry pier stability. *J Struct Eng* 1997;123:1303–11.
- [31] Krishna N, Sinha S. Behavior of Brick Masonry under Cyclic Compressive Loading. *J Constr Eng Manag* 1989;115:1432–45.
- [32] Sargin M. Stress-strain relationship for concrete and analysis of structural concrete sections. Waterloo, Canada: Univeristy of Waterloo; 1971.
- [33] de Felice G. Assessment of the load-carrying capacity of multi-span masonry arch bridges using fibre beam elements. *Eng Struct* 2009;31:1634–47. doi:10.1016/j.engstruct.2009.02.022.
- [34] Kaushik HB, Rai DC, Jain SK. Stress-Strain Characteristics of Clay Brick Masonry under Uniaxial Compression. *J Mater Civ Eng* 2007;19:728–39. doi:10.1061/(ASCE)0899-1561(2007)19:9(728).
- [35] American Concrete Institute. ACI 530. Building Code Requirements and Specification for Masonry Structures. Michigan, USA: 2013.
- [36] Kent DC, Park R. Flexural Members with Confined Concrete. *J Struct Div* 1971;97:1969–90. doi:10.1017/S000748530002229X.
- [37] Ferreira TM, Costa AA, Arede A, Gomes A, Costa A. Experimental characterization of the out-of-plane performance of regular stone masonry walls, including test setups and axial load influence. *Bull Earthq Eng* 2015;13:2667–92. doi:10.1007/s10518-015-9742-1.
- [38] Raka E, Spacone E, Sepe V, Camata G. Advanced frame element for seismic analysis of masonry structures: Model formulation and validation. *Earthq Eng Struct Dyn* 2015;44:2489–

506. doi:10.1002/eqe.2594.

- [39] Bennett RM, Boyd KA, Flanagan RD. Compressive Properties of Structural Clay Tile Prisms. *J Struct Eng* 1997;123:920–6. doi:10.1061/(ASCE)0733-9445(1997)123:7(920).
- [40] Vasconcelos G. Experimental investigations on the mechanics of stone masonry: Characterization of granites and behavior of ancient masonry shear walls. Universidade do Minho, 2005.
- [41] Pacific Earthquake Engineering Research Center (PEER). OpenSees: Open system for earthquake engineering simulation 2000.
- [42] Mander JB, Priestley MJN, Park R. Theoretical Stress-Strain Model for Confined Concrete. *J Struct Eng* 1988;114:1804–26. doi:10.1061/(ASCE)0733-9445(1988)114:8(1804).
- [43] Cavaleri L, Fossetti M, Papia M. Modeling of Out-of-Plane Behavior of Masonry Walls. *J Struct Eng* 2009;135:1522–32. doi:10.1061/(ASCE)0733-9445(2009)135:12(1522).